RSC Advances

ROYAL SOCIETY OF CHEMISTRY

PAPER

View Article Online
View Journal | View Issue

Check for updates

Cite this: *RSC Adv.*, 2023, **13**, 9978

LARP-assisted synthesis of $CsBi_3I_{10}$ perovskite for efficient lead-free solar cells†

Subbiah Vijaya, ‡[ab] Jegadesan Subbiah,*[c] David J. Jones [c] and Sambandam Anandan *[a]

Received 17th January 2023
Accepted 22nd March 2023

DOI: 10.1039/d3ra00365e

rsc.li/rsc-advances

Bismuth-based perovskites are an important class of materials in the fabrication of lead-free perovskite solar cells. Bi-based $Cs_3Bi_2I_9$ and $CsBi_3I_{10}$ perovskites are getting much attention due to their appropriate bandgap values of 2.05 eV and 1.77 eV, respectively. However, the device optimisation process plays a key role in controlling the film quality and the performance of perovskite solar cells. Hence, a new strategy to improve crystallization as well as the thin film quality is equally important to develop efficient perovskite solar cells. Herein, an attempt was made to prepare the Bi-based $Cs_3Bi_2I_9$ and $CsBi_3I_{10}$ perovskites *via* the ligand-assisted re-precipitation approach (LARP). The physical, structural, and optical properties were investigated on perovskite films deposited by the solution process for solar cell applications. $Cs_3Bi_2I_9$ and $CsBi_3I_{10}$-based perovskite-based solar cells were fabricated using the device architecture of ITO/NiO_x/perovskite layer/$PC_{61}BM$/BCP/Ag. The device fabricated with $CsBi_3I_{10}$ showed the best power conversion efficiency (PCE) of 2.3% with an improved fill factor (FF) of 69%, V_{OC} of 0.79 V, and J_{SC} of 4.2 mA cm^{-2} compared to the $Cs_3Bi_2I_9$-based device which showed a PCE of 0.7% with a FF of 47%, V_{OC} of 0.62 V and J_{SC} of 2.4 mA cm^{-2}.

Introduction

The development of Pb-free perovskite solar cells is highly demanded owing to the limitations of the practical application of Pb-based perovskite solar cells.[1] Therefore, lead-free perovskite materials are getting much attention as an alternative to the $APbX_3$ system because of the toxicity and bioaccumulation of lead in the ecosystem.[2] Metal cations such as Sn^{2+}, Sb^{3+}, and Bi^{3+} with ns² valence electron configuration are explored as the most suitable candidates to replace Pb in lead halide perovskites.[3] Among these, Sn^{2+} can be easily oxidized to Sn^{4+} which seriously affects the crystal structure, stability, and device performance. Therefore, it is worth searching for an alternative that can show similar performance to Pb-based perovskite and is stable under ambient conditions.[4] In recent years, air-stable bismuth halide perovskites are getting much attention. However, they lag behind lead halide perovskites in terms of device performance. For example, the first reported 0-D $Cs_3Bi_2I_9$ showed a PCE of 1.09%.[5] The layered bismuth halide perovskite solar cells were successfully fabricated[5–9] and proved to be one of the promising candidates to replace lead in the lead halide perovskite solar cells. In this regard, Khadka *et al.*[4] fabricated $Cs_3Bi_2I_9$-based solar cells and achieved a power conversion efficiency (PCE) of 1.26% with tailored interface and morphology. Furthermore, Shin *et al.*[6] demonstrated carbon-based bismuth halide perovskite solar cells (without using a hole transport layer) by solution route with PCE of 1.51% which opens up the way to design new solar cells. Compared to $Cs_3Bi_2I_9$, the $CsBi_3I_{10}$ exhibited a broader light absorption spectrum which is advantageous for solar cell applications. The absorption coefficient of $CsBi_3I_{10}$ is found to be 1.4×10^5 cm^{-1} with a large carrier lifetime and enhanced stability under ambient conditions.[3] Moreover, $CsBi_3I_{10}$ exhibits a narrow bandgap of 1.77 eV, which is highly demanded in the field of photovoltaics.[1] It would therefore be a good choice to consider $CsBi_3I_{10}$ as a promising alternative to Pb-based devices. Chen *et al.*[10] employed a one-step spin coating process to achieve a high-quality film of $CsBi_3I_{10}$, and the device exhibited a power conversion efficiency (PCE) of 0.32%. The film exhibited high crystallinity with few pinholes. A gas quenching-assisted anti-solvent (GQAS) technique as well as an additive strategy have been introduced to improve the crystallization and stability of $CsBi_3I_{10}$. The resulting device delivered PCE% of >1% which is one of the highest efficiencies demonstrated in the earlier reports.[1] Karim *et al.*[11] developed a $CsBi_3I_{10}$ device by introducing a bathocuproine (BCP) interfacial layer to eliminate the crystal/interfacial defects as well as to improve the interfacial

[a]Nanomaterials & Solar Energy Conversion Lab, Department of Chemistry, National Institute of Technology, Tiruchirappalli-620015, India. E-mail: sanand@nitt.edu
[b]Department of Physics, Vellore Institute of Technology, Chennai, India
[c]School of Chemistry, Bio21 Institute, The University of Melbourne, Parkville, VIC 3010, Australia. E-mail: Jsubbiah@unimelb.edu.au

† Electronic supplementary information (ESI) available: XRD, absorption spectra, of $CsBi_3I_{10}$ film. EDX of $Cs_3Bi_2I_9$. Comparison table. See DOI: https://doi.org/10.1039/d3ra00365e

‡ Equally contribute.

contact at the perovskite/electron transport layer. The device showed an efficiency of 0.80% which is higher than the control device (0.38%). Further, the device retained its initial efficiency of 90% after 528 h. According to Kang *et al.*, the gas-assisted spin coating process of $CsBi_3I_{10}$ thin film can be efficient in eliminating the poor surface morphology since the process helped to achieve high-quality $CsBi_3I_{10}$ film with large grain size. The device assembled with the [6,6]-phenyl-C61-butyric acid methyl ester (PCBM) as an electron acceptor delivered a high PCE of 1.18%.[3]

In recent years, researchers have focused on improving the device performance by tuning the bandgap, improving the film quality, morphological tuning, *etc.*[6] Khadka *et al.*[4] explored different annealing approaches such as conventional annealing (CA), antisolvent (AS), and subsequent ambient solvent vapor annealing (AS + SA) to tailor the $CsBi_3I_{10}$ film morphology. They found that the conventional annealing process of $CsBi_3I_{10}$ film resulted in poor morphology, which significantly affects the device's performance. Also found that the precursor solution supersaturation plays a key role to determine the film morphology. Further, they observed that the antisolvent dripping process produced small grains due to the rapid nucleation process. Pandiyarajan *et al.*[12] found notably improved $CsBi_3I_{10}$ perovskite film surface morphology in a one-step solution process using an anti-solvent quenching strategy. Device process condition plays a key role in controlling film quality.[1] New strategies to improve the crystallization, as well as the thin film quality are equally important to develop efficient perovskite solar cells. Among the reported methods, the anti-solvent approach has been considered effective in facilitating crystallization.[2] Further, solution-phase methods provide good control over the morphology of the $Cs_3Bi_2X_9$ (ref. 13) which significantly affects the device performance.[4] According to the literature, achieving a high-quality thin film of $CsBi_3I_{10}$ is still a challenging task.[3]

In this research work, we have investigated the solar cell device performances of $Cs_3Bi_2I_9$ and $CsBi_3I_{10}$ perovskites synthesized *via* the LARP (ligand-assisted re-precipitation) method in which DMF has been used as a 'good' solvent and toluene as a 'poor' solvent. This method has been considered one of the cost-effective and simple methods to synthesize high-quality perovskite materials under ambient conditions.[14] The prepared perovskites were fabricated into solar cell devices with the device structure of ITO/NiO_x/perovskite layer/$PC_{61}BM$/BCP/Ag. The enhanced overall performance of the device-based $CsBi_3I_{10}$ compared to $Cs_3Bi_2I_9$ has been observed.

Experimental

Materials

Cesium iodide (CsI), bismuth iodide (BiI_3), and solvents like DMF (dimethylformamide), 2-methoxy ethanol, nickel nitrate ($Ni(NO_3)_2 \cdot 6H_2O$), bathocuproine (BCP), isopropanol, chlorobenzene and toluene were purchased from Sigma-Aldrich and used as received. [6,6]-Phenyl C61 butyric acid methyl ester ($PC_{61}BM$), nano-c 99% purity solutions (2 wt%) were prepared by dissolving in anhydrous chlorobenzene (CB) at 50 °C for 7 hours.

Synthesis of $Cs_3Bi_2I_9$/$CsBi_3I_{10}$

The synthesis of $Cs_3Bi_2I_9$/$CsBi_3I_{10}$ was performed by the LARP approach. The precursor materials are highly soluble in DMF while at the same time the products $Cs_3Bi_2I_9$/$CsBi_3I_{10}$ are not soluble in toluene (since toluene is a bad solvent for $Cs_3Bi_2I_9$/$CsBi_3I_{10}$). Due to good solubility, the precursors were dissolved in DMF then this solution mixture was transferred into the 'poor' solvent (toluene) to obtain the desired product. Briefly, to synthesize $Cs_3Bi_2I_9$, 3 mmol of CsI and 2 mmol of BiI_3 were dissolved in DMF. Then this solution mixture was transferred into toluene which is taken in a beaker (under stirring). An immediate colour change from vermilion to orange was observed confirming the suspension of $Cs_3Bi_2I_9$. The stirring was continued for 30 min at room temperature. Then, the precipitate was collected by centrifugation and washed with toluene till the supernatant becomes clear. Finally, the product was dried at 80 °C in a hot-air oven overnight to evaporate the solvent. To prepare $CsBi_3I_{10}$, the same procedure was followed except that the stoichiometric ratio of 1 : 3 of CsI and BiI_3 precursors were used. The schematic representation of the LARP process to synthesize $Cs_3Bi_2I_9$ and $CsBi_3I_{10}$ have shown in the following Fig. 1.

Device fabrication

Perovskite solar cells were fabricated on ITO-coated glass substrates with a sheet resistance of 15 Ω per square. The pre-patterned ITO/glass substrates were cleaned using ultrasonication in acetone, and isopropanol each for 15 min. The wet-cleaned ITO/glass substrates were then dried using N_2 stream and exposed to the UV ozone treatment for 15 min before the film deposition. A 30 nm thick NiO_x HTL (hole transporting layer) was formed on the ITO surface by spin-coating at a rotation speed of 4000 rpm using NiO_x *precursor* solution.[19] The NiO_x HTL was then annealed at 230 °C in air for 45 min. The NiO_x-coated ITO/glass substrates were transferred into a nitrogen-purged glovebox, with oxygen and moisture levels below 0.1 ppm. The perovskite semiconductor films were formed by spin coating a precursor perovskite solution, dissolved in *N*,*N*-dimethylformamide at a concentration of 400 mg

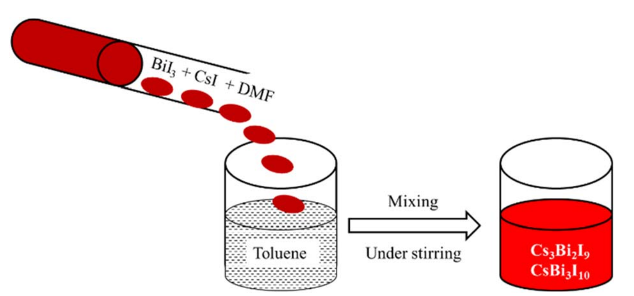

Fig. 1 Schematic representation of LARP process to synthesize $Cs_3Bi_2I_9$/$CsBi_3I_{10}$ perovskite.

mL^{-1}, on top of the NiO_x layer at 4000 rpm for the 30 s. Then the spin-coated films were then annealed at 100 °C for 10 min. Then, $PC_{61}BM$ layer (20 mg mL^{-1} in chlorobenzene) was deposited by spin coating at 2000 rpm for the 30 s. Next, the bathocuproine (BCP) interlayer was deposited using 80 μL of solution (0.05 wt% in isopropanol) by spin coating at 4000 rpm. Subsequently, a 100 nm thick Ag top electrode was deposited using thermal evaporation, with a deposition rate of 0.2 Å s^{-1}, in a vacuum chamber. The perovskite solar cells have an active area of 5.0 × 2.0 mm^2.

Characterization and measurements

The crystal structures of $Cs_3Bi_2I_9$ and $CsBi_3I_{10}$ were acquired by employing a Bruker D8 diffractometer using Cu Kα radiation (λ = 1.54 Å) at a scan rate of 0.02° min^{-1}. The morphological studies were analyzed by JEOL 7401F scanning electron microscope. A Specord S 600 diode array UV-visible spectrometer was employed to record diffuse reflectance spectroscopy. The current density–voltage measurements of the perovskite devices were carried out using a 1 kW Oriel solar simulator with an AM 1.5G filter as the light source in conjunction with a Keithley 2400 source measurement unit. Solar measurements were carried out under 1000 W m^{-2} AM 1.5G illumination conditions. For accurate measurement, the light intensity was calibrated using a reference silicon solar cell (PV Measurements Inc.) certified by the National Renewable Energy Laboratory. Device fabrication and characterizations were performed in a glove box without any encapsulation. The photovoltaic parameters are derived from J–V plot, and FF was calculated using the following equation, FF $= J_{mpp} \times V_{mpp}/J_{SC} \times V_{OC}$. where, J_{mpp} and V_{mpp} and current density and voltage at maximum power point condition.

Results and discussions

The XRD pattern of both $Cs_3Bi_2I_9$ and $CsBi_3I_{10}$ are shown in Fig. 2. The formation of $Cs_3Bi_2I_9$ has been compared with the available JCPDS card no. 01-089-1846, whereas the crystal system of the $CsBi_3I_{10}$ has been compared with the previously reported literature,[15] since JCPDS card no. for reference pattern of $CsBi_3I_{10}$ is not available.

The XRD pattern of $Cs_3Bi_2I_9$ shown in Fig. 3, reveals that the crystal structure belongs to a hexagonal geometry (space group $P6_3/mmc$) with the lattice constants of $a = 8.40$, $b = 8.40$, $c = 21.24$ Å (JCPDS card no. 01-089-1846) having two Bi^{3+} ions in the unit cell. The face sharing of two $[BiI_6]^{3-}$ octahedra forms and $[Bi_2I_9]^{3-}$ bi-octahedra eventually ended with the 0-D crystal structure. The Cs^+ ions fill the voids present in those bi-octahedra.[16] The peaks observed at 12.8°, 21.1°, 24.3°, 25.1°, 25.8°, 27.5°, 29.7°, 32.3°, 36.9°, 38.5°, 42.1°, 42.9°, 45.8°, 50.4°, 51.7°, 53.0°, 54.8°, 69.4° are corresponding to the planes of (1 0 1), (1 1 0), (1 0 5), (0 0 6), (2 0 2), (2 0 3), (2 0 4), (2 0 5), (2 1 4), (2 0 7), (2 0 8), (2 2 0), (2 0 9), (2 2 6), (4 0 3), (4 0 4), (4 0 5), (3 3 4), respectively. The observed XRD pattern of the $Cs_3Bi_2I_9$ well matches with the reference pattern (JCPDS card no. 01-089-1846), which confirms the formation of the same. The XRD pattern of $CsBi_3I_{10}$ reveals the most significant peaks (asterisk symbol shown in Fig. 2) at 12.8, 25.1, 25.8, 41.6 which correspond to the (0 0 3), (0 0 6), (1 1 5), (3 0 0) planes respectively. Further, many peaks corresponding to $Cs_3Bi_2I_9$ have been found in the XRD pattern of $CsBi_3I_{10}$. It should be noted that the crystal structure of $CsBi_3I_{10}$ is comparable to the crystal structure of BiI_3 and $Cs_3Bi_2I_9$ which are stable secondary and ternary phases.[17] In addition to this, the XRD pattern of $CsBi_3I_{10}$ deposited on the glass also confirms the presence of (0 0 3), (0 0 6), (1 1 5), (3 0 1) planes in the crystal lattice (Fig. S1†).

The diffuse reflectance spectroscopy (DRS) of $Cs_3Bi_2I_9$ shows (Fig. 3a) a bandgap of 2.05 eV which is in good agreement with the theoretically calculated bandgap value.[18] The characteristic absorption peak at 488 nm has been observed in the UV-vis spectrum of $Cs_3Bi_2I_9$ (Fig. 3b). The range of visible light absorption has been found to extend up to 623 nm. Compared to $Cs_3Bi_2I_9$, the bandgap of $CsBi_3I_{10}$ has been reduced to 1.72 eV (shown in Fig. 3c), which causes extended light absorption. The absorption spectra of $CsBi_3I_{10}$ film recorded before (at room

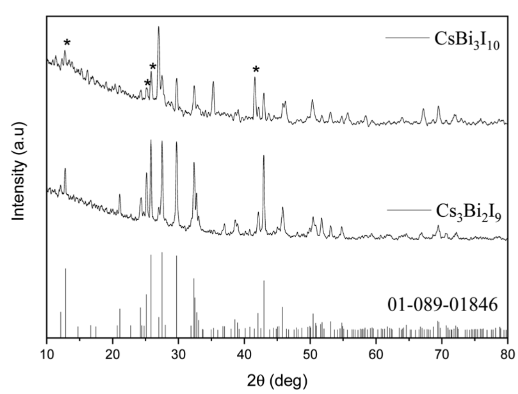

Fig. 2 XRD pattern of $Cs_3Bi_2I_9/CsBi_3I_{10}$ compared with the JCPDS card no. 01-089-1846 (* denote most significant peaks).

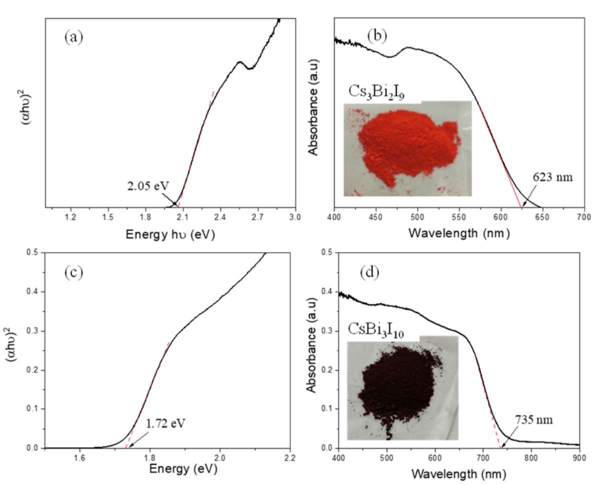

Fig. 3 (a, c) DRS and (b, d) absorption spectra of $Cs_3Bi_2I_9$ and $CsBi_3I_{10}$ respectively, (inset photograph shows the respective perovskite samples).

temperature) and after annealing (100 °C) are shown in Fig. S2a.† The dark colour of the $CsBi_3I_{10}$ layer can be visibly seen in the images shown in Fig. S2b and c (ESI†).

Morphological study

The FE-SEM images of $Cs_3Bi_2I_9$ power with different magnifications are shown in Fig. 4a and b. The images show the morphology of the $Cs_3Bi_2I_9$ appears to be hexagonal flakes-like shapes with low-dimension. The thickness of the flakes is found to be around 30 nm which is perpendicular to the surface. Further, the elemental presence of Cs, Bi, and I in $Cs_3Bi_2I_9$ has been confirmed from the EDX image shown in Fig. S3.† The surface morphology of the $CsBi_3I_{10}$ films after annealing show the well-defined perovskite crystal with enhanced morphology (Fig. 5a–d). The EDX image of both $Cs_3Bi_2I_9$ (powder) and $CsBi_3I_{10}$ perovskite film layer (after annealing at 100 °C) shown in Fig. S3† confirm the elemental presence of the components Cs, Bi, and I, respectively. The difference in the stoichiometry ratio (Fig. S3a†) might be due to the presence of secondary and ternary phase in the sample. The presence of indium and silicon (Fig. S3b†) element along with Cs, Bi, and I comes from the ITO/glass substrate (since EDX has been recorded for $CsBi_3I_{10}$ film coated on glass/ITO substrate after annealing 100 °C).

J–*V* characterization

The schematic representation of the device structure is shown in Fig. 6a. *J*–*V* measurements of the perovskite solar cell devices fabricated with $Cs_3Bi_2I_9$, and $CsBi_3I_{10}$ (before and after annealing) have been depicted in Fig. 6b and the *J*–*V* parameters are shown in Table 1. The device structure adopted in this work is ITO/NiO_x/perovskite layer/$PC_{61}BM$/BCP/Ag. As shown in Fig. 6b, the device fabricated with $Cs_3Bi_2I_9$ delivered a power conversion efficiency (PCE) of 0.7% with a FF of 47, V_{OC} of 0.62 V, and J_{SC} of 2.4 mA cm^{-2}. The poor performance of the device might be due to the discrete nature of the $[Bi_2I_9]^{3-}$ bioctahedra as well as bulk recombination even though $Cs_3Bi_2I_9$ has a long charge carrier lifetime.[16] The device fabricated with $CsBi_3I_{10}$ before annealing delivered the PCE of 0.15% with FF of 34%, V_{OC} of 0.40 V, and J_{SC} of 1.1 mA cm^{-2}. The poor performance of the device is due to the absence of perovskite structure formation. Finally, the device fabricated with annealed $CsBi_3I_{10}$ showed the best performance efficiency of 2.3% with improved FF of 69%, V_{OC} of 0.79 V, and J_{SC} of 4.2 mA cm^{-2}. Upon annealing 100 °C, the $CsBi_3I_{10}$ film changes color from orange-red to blackish (Fig. S2–c†) with compact and large grain morphology. Compared to $Cs_3Bi_2I_9$, the enhanced performance of $CsBi_3I_{10}$ perovskite-based device due to improved surface morphology, reduced interface energy barrier, and efficient interfacial charge extraction.[16] In addition to this, the broader light absorption of $CsBi_3I_{10}$ compared to $Cs_3Bi_2I_9$ which is evidenced by the UV-vis absorption spectra shown in Fig. 3d, enhances the generation of photocurrent of the $CsBi_3I_{10}$-based perovskite solar cell device. Furthermore, the usage of the BCP layer in the device architecture facilitates hole blocking with enhanced electron extraction at the cathode (PCBM/BCP/Ag) interface.[12]

Modifying the surface morphology and the film quality are most common way to improve the device performance.[6] In this regard, researchers attempted to fabricate the $CsBi_3I_{10}$ film *via* spin coating and thermal annealing process to improve the surface morphology. In this work, the $CsBi_3I_{10}$ perovskite prepared from LARP assisted synthesis shows well-defined perovskite crystal with hexagonal flakes-like morphology which is desirable for the device performance. The results from this work reveal that LARP assisted synthesis can improve the film quality and morphology. Further, the utilization of hole extraction layer (NiO_x nanoparticle) and hole blocking layer (BCP) facilitate the extraction of electron at the electrode interface[12] which simultaneously enhances the overall

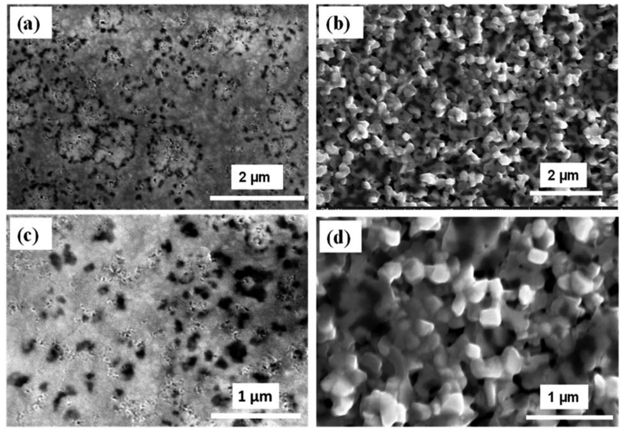

Fig. 5 (a, c) SEM images of $CsBi_3I_{10}$ film before annealing (b, d) after annealing.

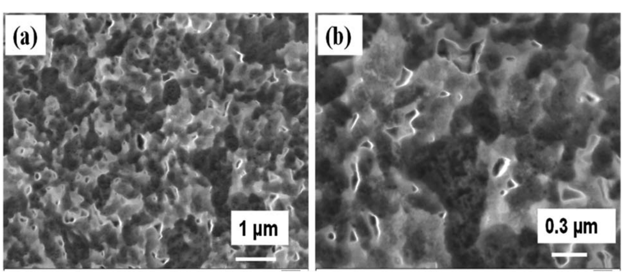

Fig. 4 (a and b) SEM images of $Cs_3Bi_2I_9$.

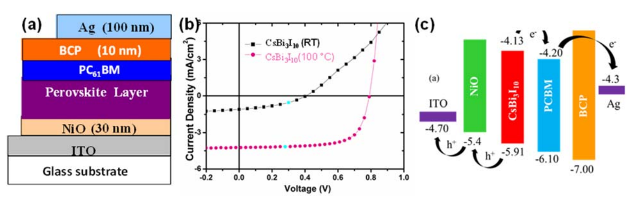

Fig. 6 (a) Schematic of perovskite solar cell (b) *J*–*V* measurements of perovskite devices fabricated with $CsBi_3I_{10}$ (before and after annealing) and (c) energy level diagram of device components of perovskite solar cell.

Table 1 Device characteristics of perovskite solar cells fabricated with $Cs_3Bi_2I_9$ and $CsBi_3I_{10}$

Perovskite layer	J_{SC} (mA cm^{-2})	V_{OC} (V)	FF (%)	PCE%
$Cs_3Bi_2I_9$ (before annealing)	2.2	0.60	45	0.60
$Cs_3Bi_2I_9$ (after annealing)	2.4	0.62	47	0.70
$CsBi_3I_{10}$ (before annealing)	1.1	0.40	34	0.15
$CsBi_3I_{10}$ (after annealing)	4.2	0.79	69	2.30

performance of the device. The $Cs_3Bi_2I_9$ and $CsBi_3I_{10}$ perovskite-based solar cell performances of the previously reported literature have been compared and shown in Table S1 (ESI†). It is evidenced that the $CsBi_3I_{10}$ perovskite synthesized *via* the LARP approach delivered the best overall performance along with improved FF among all the previous reports.

Conclusions

Herein, we demonstrated the LARP approach to the synthesis of highly efficient $CsBi_3I_{10}$ perovskite for solar cell application. The XRD pattern of $CsBi_3I_{10}$ showed the presence of secondary and ternary phases within it. The SEM images of $CsBi_3I_{10}$ showed improved morphology and crystallinity compared to $Cs_3Bi_2I_9$. The device based on $CsBi_3I_{10}$ showed the best overall performance efficiency of 2.3%. The device fabricated with $Cs_3Bi_2I_9$ showed a PCE of only 0.7%. The presence of excess BiI_3 in the $CsBi_3I_{10}$ improved the performance efficiency by suppressing the intrinsic defects of the device. The higher absorption of $CsBi_3I_{10}$ in the extended UV-vis region compared to $Cs_3Bi_2I_9$ helped to improve the J_{SC} value of the device. Further, the device architecture ITO/NiO_x/perovskite layer/$PC_{61}BM$/BCP/Ag in which the BCP helps to block the unwanted hole leakage at the $CsBi_3I_{10}$/PCBM interface by improving the charge transport process in the device. This work paves the way to achieving high-performance $CsBi_3I_{10}$ perovskite solar cells.

Conflicts of interest

There are no conflicts to declare.

Acknowledgements

Author SV thanks the DST-WOS-A (SR/WOS-A/CS-78/2017). Author SA thanks the SPARC scheme (SPARC/2018-2019/P236/SL) for the financial assistance. JS and DJJ acknowledge the support of the Australian Government through the Australian Renewable Energy Agency (ARENA) and the Australian Centre for Advanced Photovoltaics (ACAP). The Australian Government does not accept responsibility for the views, information or advice expressed herein.

References

1 J. Deng, L. Yang, X. Zhang, K. Wei, G. Du, G. Zhu and J. Zhang, *J. Mater. Chem. A*, 2022, **10**(17), 9384–9392.
2 J. Shamsi, A. S. Urban, M. Imran, L. De Trizio and L. Manna, *Chem. Rev.*, 2019, **119**(5), 3296–3348.
3 J. Kang, J. Liu, O. Allen, M. Al-Mamun, P. Liu, H. Yin, Y. Wang, S. Chen and H. Zhao, *Energy Technol.*, 2022, **10**(7), 2200318.
4 D. B. Khadka, Y. Shirai, M. Yanagida and K. Miyano, *J. Mater. Chem. C*, 2019, **7**(27), 8335–8343.
5 B. W. Park, B. Philippe, X. Zhang, H. Rensmo, G. Boschloo and E. M. Johansson, *Adv. Mater.*, 2015, **27**(43), 6806–6813.
6 J. Shin, M. Kim, S. Jung, C. S. Kim, J. Park, A. Song, K. B. Chung, S. H. Jin, J. H. Lee and M. Song, *Nano Res.*, 2018, **11**(12), 6283–6293.
7 B. B. Yu, M. Liao, J. Yang, W. Chen, Y. Zhu, X. Zhang, T. Duan, W. Yao, S. H. Wei and Z. He, *J. Mater. Chem. A*, 2019, **7**(15), 8818–8825.
8 M. B. Johansson, B. Philippe, A. Banerjee, D. Phuyal, S. Mukherjee, S. Chakraborty, M. Cameau, H. Zhu, R. Ahuja, G. Boschloo and H. Rensmo, *Inorg. Chem.*, 2019, **58**(18), 12040–12052.
9 M. B. Johansson, H. Zhu and E. M. Johansson, *J. Phys. Chem. Lett.*, 2016, **7**(17), 3467–3471.
10 X. Y. Chen, H. B. Lan, G. X. Liang and P. Fan, *Photonics for Energy*, Optica Publishing Group, 2018, p. PT4B-28.
11 M. Karim, K. Matsuishi, T. H. Chowdhury, W. I. Chowdhury, M. Abdel-shakour and A. Islam, *J. Mater. Sci.: Mater. Electron.*, 2022, **33**(10), 8114–8126.
12 P. Mariyappan, T. H. Chowdhury, S. Subashchandran, I. Bedja, H. M. Ghaithan and A. Islam, *Sustainable Energy Fuels*, 2020, **4**(10), 5042–5049.
13 R. F. Ali, I. Andreu and B. D. Gates, *Nanoscale Adv.*, 2019, **1**(11), 4442–4449.
14 J. Shamsi, A. S. Urban, M. Imran, L. De Trizio and L. Manna, *Chem. Rev.*, 2019, **119**(5), 3296–3348.
15 P. Sebastia-Luna, M. C. Gélvez-Rueda, C. Dreessen, M. Sessolo, F. C. Grozema, F. Palazon and H. J. Bolink, *J. Mater. Chem. A*, 2020, **8**(31), 15670–15674.
16 B. Ghosh, B. Wu, H. K. Mulmudi, C. Guet, K. Weber, T. C. Sum, S. Mhaisalkar and N. Mathews, *ACS Appl. Mater. Interfaces*, 2018, **10**(41), 35000–35007.
17 X. W. Tong, Z. X. Zhang, D. Wang, L. B. Luo, C. Xie and Y. C. Wu, *J. Mater. Chem. C*, 2019, **7**(4), 863–870.
18 K. M. McCall, C. C. Stoumpos, O. Y. Kontsevoi, G. C. Alexander, B. W. Wessels and M. G. Kanatzidis, *Chem. Mater.*, 2019, **31**(7), 2644–2650.
19 Z. Liu, J. Chang, Z. Lin, L. Zhou, Z. Yang, D. Chen, C. Zhang, S. Liu and Y. Hao, *Adv. Energy Mater.*, 2018, **8**(19), 1703432.